Research Article

GAZİ
JOURNAL OF ENGINEERING SCIENCES

Numerical Investigation of Laser Power Effects on Thermal Distribution and Melt Pool Morphology in Laser Powder Bed Fusion of 316L Stainless Steel

Oğulcan EREN[*a]

Submitted: 24.11.2025 **Revised :** 18.12.2025 **Accepted:** 26.12.2025 **doi:**10.30855/gmbd.070525AR13

[a,*] Gazi University, Technology Faculty, Dept. of Industrial Design Engineering 06560 - Ankara, Türkiye, Orcid: 0000-0003-1904-1868
Corresponding author: ogulcaneren@gazi.edu.tr

Keywords:
Laser Powder Bed Fusion (LPBF), Finite Element Method (FEM), Melt pool morphology, thermal distribution, additive manufacturing

ABSTRACT

Laser Powder Bed Fusion (LPBF) is a widespread additive manufacturing method for precisely fabricating intricate metal parts. Despite its advantages, this process is highly sensitive to laser parameters, especially laser power, which determines the thermal behavior and the properties of the melt pool. In this study, transient finite element thermal analysis is presented to investigate the effect of varying laser power, quantified through Volumetric Energy Density (VED), on the temperature distribution and melt pool morphology in 316L stainless steel. This moving Gaussian laser transient thermal model implemented using Ansys Workbench was used to simulate single-track laser scanning. Unlike other complex finite element models, this simplified model is a practical tool that allows to predict thermal distribution in a computationally efficient manner. The results demonstrate that increasing VED leads to higher surface temperatures and deeper melt pools, transitioning from conduction-mode to keyhole-mode melting. Specifically, low VED conditions produced shallow melt pools that risk lack-of-fusion defects, while high VED resulted in geometries indicative of vaporization and keyhole instability. The research provides practical guidance on optimal power configurations and emphasizes the effectiveness of reduced-order thermal models for swift parametric analysis in LPBF.

1. Introduction

Additive manufacturing (AM) is a process that builds a three-dimensional object by adding material layer by layer. Among various additive manufacturing technologies, Laser Powder Bed Fusion (LPBF), commonly referred to as Selective Laser Melting (SLM), is emerging as a promising technique for the production of complex metallic components characterized by high density and enhanced mechanical properties [1]. This technology enables the production of parts with improved mechanical properties by selectively melting metal powders with a high-energy laser beam according to digital design data [2]. LPBF has become widely used, particularly in the aerospace, biomedical, and automotive industries, due to its ability to increase material efficiency, reduce weight through lattice structures, and enable industrial automation [3, 4]. However, despite this transformative potential, the industrial viability of LPBF is frequently hindered by challenges related to process repeatability, surface quality, and the presence of intrinsic defects such as porosity and residual stresses [5, 6]. This is because the physical phenomena governing the LPBF process are inherently complex. The process involves rapid heating and cooling cycles, phase transformations, and severe fluid dynamics within the microscopic melt pool [7, 8]. The quality of the final component is dictated by numerous process parameters, including laser power, scanning speed, hatch spacing, and layer thickness [9]. The interplay between these parameters governs the thermal history of the part, thereby determining microstructure evolution and mechanical performance. For instance, thermal gradients and solidification

To cite this article: O. Eren, "Numerical Investigation of Laser Power Effects on Thermal Distribution and Melt Pool Morphology in Laser Powder Bed Fusion of 316L Stainless Steel", *Gazi Journal of Engineering Sciences,* vol.11, no.3, pp. 481-494, 2025. doi:10.30855/gmbd.070525AR13

rates within the melt pool directly influence dendrite arm spacing and grain morphology, which are critical factors of strength and hardness [10]. Furthermore, melt pool stability is crucial. Instabilities driven by surface tension gradients or recoil pressure can lead to severe defects such as balling, spatter, and keyhole porosity [11].

Among LPBF parameters, laser power is one of the most important factors in governing the thermal environment and melt pool characteristics during fabrication. Laser power, along with scanning speed, scanning range, and layer thickness, determines the energy delivered per unit material volume and is typically expressed as Volumetric Energy Density (VED) in J/mm³. VED is a convenient single metric that combines key parameters and is frequently used to compare processing conditions or predict part quality across studies. Chen et al. reported that 316L LPBF process results are highly sensitive to energy input. They observed that adjusting the VED significantly altered single-track and double-track formation and determined an optimum VED range that minimizes defect formation in 316L builds [12]. Likewise, numerous experimental studies confirm the significant impact of laser energy parameters. For example, Cherry et al. [13] varied point exposure and Liverani et al. [14] varied laser power and scan strategy, both reporting substantial effects on the porosity, microstructure, and mechanical properties of 316L parts. Bakhtiarian et al. demonstrated through a design-of-experiments approach that laser power, scan speed, and layer thickness (factors which collectively determine VED) significantly affect the density and hardness of 316L specimens. In their study, an intermediate energy density of about 125 J/mm³ (achieved with 180 W power, 1200 mm/s speed, 30 μm layers) produced a ~99.5% dense part with high hardness, whereas lower energy inputs led to lack of fusion porosity and higher inputs induced keyhole porosity [15]. Fri et al. further showed that the VED–property relationship in 316L is non-linear: the Vickers hardness follows a concave trend with respect to VED, peaking at ~166 J/mm³ and dropping off at higher energies due to thermal accumulation and in-process annealing effects. They observed an exponential decrease in porosity as VED increased, up to that optimum point [16]. These studies collectively highlight that there exists a process window for energy input: too low laser power (or insufficient VED) causes incomplete melting and defects, while too high power (excessive VED) causes overheating, vaporization, and melt instability – both extremes leading to degraded part quality. Achieving the right balance of laser power and scan parameters is therefore critical to obtain stable melt pool dynamics and high-quality 316L builds.

To better understand and optimize such process parameters, numerical simulation has emerged as a powerful tool alongside experiments. Conducting iterative experiments to find optimal laser settings is costly and time-consuming, whereas simulations can provide insight into melt pool thermal behavior more efficiently. Over the past decade, a range of computational models have been developed for LPBF. At one end of the spectrum are high-fidelity multiphysics models that attempt to capture the detailed physics of the melt pool, including laser–material interaction, rapid melting/solidification, fluid flow driven by surface tension (Marangoni convection), recoil pressure, and even evaporation/solidification phase changes. For instance, Mukherjee et al. implemented a comprehensive 3D transient heat transfer and fluid flow model for powder bed fusion, which can predict melt pool temperature and velocity fields, pool shape and size, cooling rates, and solidification parameters for various alloys including 316L [17]. Such high-resolution models, often validated by experiments, can provide deep insight into phenomena like keyhole formation and dendritic microstructure evolution under different laser powers [18]. However, the inclusion of melt pool convection and other complex physics comes at the cost of enormous computational effort. Solving the Navier–Stokes equations for fluid flow alongside heat transfer in a moving melt pool demands fine spatial/temporal resolution and substantial computing resources. This complexity makes multiphysics simulations impractical for rapid process optimization or routine industrial use – especially when a large parameter space (e.g. various laser powers and scan speeds) must be explored.

On the other end of the modeling spectrum, researchers have explored simplified thermal models that trade some physical accuracy for drastically improved computational efficiency. These models treat the laser melting process primarily as a transient heat conduction problem, ignoring fluid flow and other multi-phase phenomena. Despite the simplifications, they can still capture first-order thermal trends and melt pool geometry responses to process parameters. For example, Foteinopoulos et al. developed a two-dimensional finite difference model with an adaptive meshing (node birth) technique to simulate the temperature evolution in SLM, managing to reduce computation time while reasonably predicting melt pool dimensions and cooling rates [19]. Such reduced-order models are well-suited for scanning a broad range of conditions to identify general process windows. Ansari et al. similarly proposed a computationally efficient thermal model to study heat accumulation effects in metal powder bed fusion. Their model, based on Fourier's heat conduction formulation, provided accurate thermal profiles for single and multiple tracks while maintaining low computational overhead, confirming that simplified models can reliably guide parameter selection for industrial LPBF applications [20]. In conclusion, simplified thermal models serve as highly practical tools for understanding and comparing LPBF process behavior. By significantly reducing computational cost, these models enable rapid assessment of parameter trends and melt pool responses, particularly with respect to laser power and energy input. Such fast evaluations allow designers and process engineers to perform early-stage screening and preliminary optimization before resorting to more complex experiments or high-fidelity multiphysics simulations. This capability directly supports agile

ISSN: 2149-9373 © 2025 Parantez Academic Publishing All rights reserved

process development in industrial LPBF applications, where short iteration cycles, fast feedback, and efficient decision-making are often more critical than resolving all fine-scale physical phenomena at the initial design stage.

In this study, a transient thermal finite-element analysis is employed to investigate the effect of laser power on the thermal distribution and melt pool morphology in LPBF of 316L stainless steel. Unlike many prior numerical works that incorporate fluid flow or complex multi-physics, proposed model focuses only on heat transfer, omitting phenomena such as Marangoni convection, vaporization, and melt pool dynamics. This simplification yields a computationally efficient simulation framework that can provide prompt predictions of melt pool dimensions and peak temperatures under different processing conditions. The novelty of this study lies in demonstrating that such a simplified model can still capture the fundamental trends regarding the effect of energy input on the melt pool geometry and provide a quick and practical method for process parameter evaluation. Three laser power settings – 120 W, 180 W, and 240 W – which correspond to VED values of approximately 83, 125, and 167 J/mm^3, respectively, has been examined. These conditions span from a low energy input (prone to lack-of-fusion) through an intermediate optimum, up to a high energy input approaching keyhole regimes. By comparing the simulated melt pool dimensions (width and depth) and thermal profiles at these power levels, the relationship between laser power (and consequently VED) and melt pool morphology in 316L has been established. The results of this study contribute to refining the process parameter space in LPBF by demonstrating that excessive laser power can lead to diminishing returns and compromise melting pool stability. The proposed thermal model serves as a rapid and computationally efficient tool for preliminary screening of laser parameters, offering valuable support for process planning and experimental optimization in the fabrication of 316L and similar alloys.

2. Finite Element Modelling

2.1. Modeling assumptions and geometrical representation

The laser powder bed fusion process is modeled using a three-dimensional finite element transient thermal analysis in ANSYS Workbench. The simulation domain represents a small section of the build, including a 316L stainless steel substrate and a thin layer on top. A cartesian coordinate system was defined, with the x-y plane corresponding to the powder bed surface and the z plane corresponding to the build direction (vertical). A typical thickness of 30 μm was assigned to the powder layer to represent a single LPBF layer. The layer and the underlying substrate were modeled as a continuous solid with the effective thermophysical properties of 316L stainless steel. Symmetric boundary conditions and a sufficiently large area were selected to ensure that heat flow at the edges would minimally affect the melt pool region. Initially, the entire area was set to room temperature, and convective and radiative heat losses were applied to the free surfaces to provide a cooling effect to the surrounding environment. Figure 1 schematically illustrates these thermal interactions. When a Gaussian laser beam strikes a powder bed, some of its energy is reflected, depending on the material properties. The remaining energy is converted to heat.

Laser irradiation is simulated as a moving volumetric heat source within the powder layer, following the Beer–Lambert law for energy absorption. The laser travels along a prescribed scan path on the powder surface with a constant scan speed, depositing heat as it moves. A Gaussian distribution is assumed for the beam profile in the horizontal plane, while exponential attenuation is applied through the depth of the powder layer. In mathematical terms, the heat intensity distribution (power per unit volume) is defined as Eq. 1.

$$I(r,z) = I_0 \exp\left(-\frac{2r^2}{{w_0}^2}\right) exp(-\beta z) \quad (1)$$

Where r is the radial distance from the laser center, and z is the depth below the powder surface [21]. Here w_0 is the laser beam radius and β is the absorption coefficient characterizing the Beer–Lambert attenuation in 316L powder. The peak laser intensity I_0 at the surface center is expressed as Eq. 2, which depends on the laser power P and the material absorptance η (fraction of incident laser energy that is absorbed) and spot size (w_0).

$$I_0 = \frac{2\eta P}{\pi w^2} \quad (2)$$

ISSN: 2149-9373 © 2025 Parantez Academic Publishing All rights reserved

This formulation allows for volumetric deposition of laser energy. The Gaussian term distributes the power across the beam spot, while the *exp(-βz)* term accounts for energy absorption within the powder layer thickness.
The moving heat source is implemented via user-defined functions and ANSYS APDL scripts to update the location of *I(r,z)* as the laser scans over time. This approach captures the formation of a roughly ellipsoidal melt region in the substrate and powder, corresponding to a conduction-mode melt pool beneath the laser.

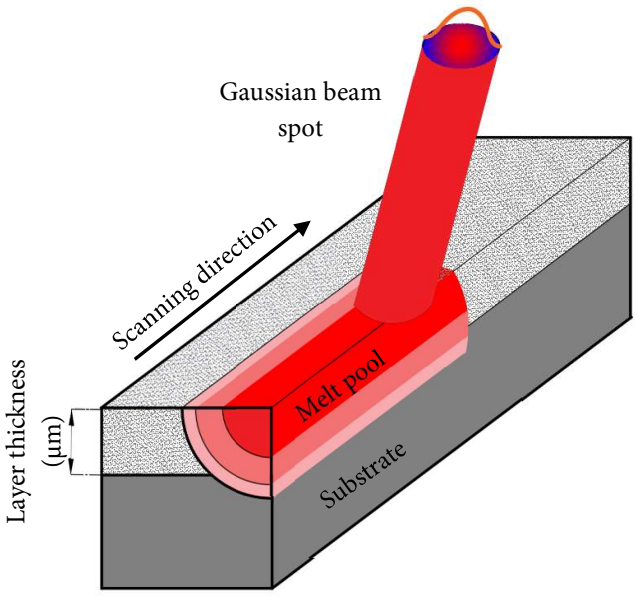


Figure 1. Schematic of laser powder bed fusion process. Reproduced from [22]

Several modeling simplifications have been adopted to make the simulation computationally efficient. The model focuses on heat transfer via conduction and neglects the complex fluid flow and phase change events occurring in the actual melting pool. Thus, the computation time for a single tracing simulation has been reduced from several hours, required by fully coupled multi-physics models [22], to approximately 12 minutes using the current thermal-only formulation. This significant reduction in analysis time enables rapid parametric evaluation and enhances the model's suitability for industrially agile LPBF process development. In particular, the following effects have been neglected:

1) No surface-tension-driven flow is modeled in the melt pool.
2) The model does not explicitly simulate melting/solidification kinetics or the latent heat of fusion. The material is assumed to undergo a continuous increase in temperature without a discrete solid-liquid phase transition.
3) The melt pool is not treated as a moving fluid. There is no hydrodynamic simulation of liquid metal; instead, the molten region is treated as an element of the solid domain with enhanced thermal conductivity. This means convective heat transport within the melt is not explicitly captured.
4) High-power laser phenomena like metal vaporization, recoil pressure, and keyhole formation are not considered. No vapor plume or laser penetration beyond the optical attenuation length is modeled.

2.2. Governing equations

The thermal field generated during the laser powder bed fusion process is obtained by solving the three-dimensional transient heat conduction equation using the ANSYS Transient Thermal module. Since the model employs a purely thermal formulation, heat transfer occurs exclusively through conduction within the solid domain and convection at exposed boundaries. Fluid flow, Marangoni effects, recoil pressure, and phase-change kinetics are intentionally excluded from the governing physics to achieve high computational efficiency. The temperature evolution *T(x,y,z,t)* is described in Eq 3.

ISSN: 2149-9373 © 2025 Parantez Academic Publishing All rights reserved

$$\rho(T)\ c_p(T)\frac{\partial T}{\partial t} = \nabla.\left[k(T)\nabla \mathrm{T}\right] + Q(x,y,z,t) \quad (3)$$

Here $\rho(T)$ is temperature-dependent density, $c_p(T)$ is temperature-dependent specific heat capacity, $k(T)$ denotes temperature-dependent thermal conductivity and $Q(x,y,z,t)$ is applied volumetric heat input.

During LPBF, the build chamber is filled with argon gas, which provides inert protection while also influencing heat loss. Convective heat transfer at open surfaces is modeled using a temperature-dependent convection coefficient *h(T)* of argon provided by the materials library in ANSYS. Convective heat loss at all free surfaces is expressed in Eq. 3.

$$-k(T)\,\nabla T \cdot \mathrm{n} = h(T)\,[T - T_\infty] \quad (4)$$

Where $h(T)$ denotes temperature-dependent convection coefficient (W/m^2·°C), T_∞ is argon ambient temperature in the build chamber and n is outward normal vector of the surface. This formulation accounts for cooling driven by argon flow and natural convection within the chamber environment. Higher surface temperatures correspond to increased convective heat extraction, which is essential for capturing realistic cooling rates after laser passage.

2.3. Gaussian heat source

In the numerical model, the laser is represented as a moving three-dimensional Gaussian volumetric heat source acting within the powder layer and the upper region of the substrate. The spatial and temporal distribution of the absorbed heat is defined as Eq. 5. In this equation, the laser absorptivity of the 316L powder bed is assumed to be constant and taken as η = 0.63. This value was selected as a representative effective absorptivity for stainless steel powder beds and lies within the range commonly reported in LPBF literature [23].

$$Q(x,y,z) = \frac{2\eta P}{\pi {w_0}^2 \Delta} exp\left[-2\frac{\left[x-(x_0+v_b\cdot t)^2+(y-y_0)^2\right]}{{w_0}^2}\right] exp\left[-\frac{|z|}{\Delta}\right] \quad (5)$$

Where $Q(x,y,z,t)$ is the volumetric heat source (W/mm^3) η is the absorption efficiency of 316L powder, P is the laser power (W), w_0 is the radius of the laser beam at the powder surface (mm), Δ is the effective optical penetration depth (mm), (x_0, y_0) is the initial position of the laser beam center at $t = 0$, v_b is the laser scan speed along the x-direction (mm/s), z is the depth coordinate measured from the top surface (mm).

The first exponential term describes the Gaussian distribution in the scanning plane. At any time t, the laser center is located at $x_c(t) = x_0 + v_b t$, and the heat flux decays radially away from this center in both x and y directions with a characteristic radius w_0. This reproduces the typical circular laser spot with maximum intensity at the beam center and rapid decay toward the edges. The second exponential term $exp(-|\ z\ |/\Delta)$ accounts for Beer–Lambert–type attenuation in the depth direction, assuming that the laser intensity decays exponentially as it penetrates into the powder layer and the underlying solid. The parameter Δ therefore represents the effective penetration depth over which most of the laser energy is deposited within the material.

The moving Gaussian heat source was implemented in ANSYS using an APDL-based formulation in which the volumetric heat input is defined through a user-generated table function. The APDL script evaluates the spatial Gaussian expression at each time step by accessing the nodal coordinates and the current simulation time. The expression follows the time-dependent moving gaussian heat source equation given in Eq. 5. This function is encoded through a series of *set commands that define the polynomial coefficients of the table array HEAT_FLX1, enabling ANSYS to compute the Gaussian intensity distribution in real time during the transient analysis. The function contains a set of commands that apply the calculated heat flux directly to specified surface elements. In this manner, the laser heat source travels across the domain while maintaining the Gaussian spatial distribution. The APDL routine therefore enables a fully time-dependent, moving laser input without requiring external user subroutines, and ensures that the transient thermal solution captures the thermal gradients produced by the scanning laser. The APDL script used in the study is provided in the Appendix.

ISSN: 2149-9373 © 2025 Parantez Academic Publishing All rights reserved

2.4. Material properties

Accurately defining temperature-dependent material properties is crucial for reliable heat transfer simulations in LPBF. The thermal response of the melt pool and the surrounding powder/solid material is highly sensitive to properties such as thermal conductivity and specific heat, which govern heat flow and energy storage in the material. In this study, the thermophysical properties of 316L stainless steel were obtained from the ANSYS Engineering Data Materials Library and validated with literature data [24]. The properties were defined over a broad temperature range (25–3725 °C) to encompass the entire process, from room-temperature powder to the highest transient temperatures under the laser. Table 1 summarizes the key physical properties of 316L as a function of temperature.

Table 1. Physical properties of 316L [24]

Property	**Unit**	**25 °C**	**1425 °C**	**3725 °C**
Density (ρ)	kg/m^3	8000	7700	-
Specific heat (C_p)	J/kg.K	500	600	950
Thermal conductivity (k)	W/m.K	14	30	44
Dynamic Viscosity (μ)	Pa.s	-	$6.7\text{x}10^{-3}$	-
Thermal expansion (β)	K^{-1}	$16\text{x}10^{-6}$	$18\text{x}10^{-6}$	-
Solidus temp. (T_s)	°C		1375	
Liquidus temp. (T_l)	°C		1450	
Vaporization temp. (T_v)	°C		2800	
Emissivity (ε)	-		0.3	
Absorption (η)	-		0.63	
Initial temp. (T_0)	°C		23	

In addition to the alloy properties, the characteristics of the argon shielding gas were incorporated for boundary heat loss modeling. High-purity argon is the standard inert atmosphere used in LPBF to prevent oxidation [25]. In the simulation, convective and radiative heat transfer coefficients were applied at free surfaces to represent cooling by the argon environment. The convective behavior of argon governs the heat lost from the sample by convection [26], although conduction within the metal dominates the overall heat dissipation. By using argon's properties to set an appropriate convection coefficient and ambient conditions, the model accounts for heat losses to the surrounding gas, ensuring a realistic thermal boundary condition consistent with the LPBF process.

2.5. Transient simulation model and boundary conditions

The numerical model was developed using the transient thermal module in ANSYS to investigate laser-induced thermal behavior in LPBF. The computational domain consists of a thin powder layer deposited on a bulk 316L stainless steel substrate. The laser is modeled as a continuously moving three-dimensional volumetric Gaussian heat source with exponential depth decay, implemented using APDL expressions based on the Beer–Lambert law. The laser motion is defined as a continuous function of time through the scanning term in the heat source formulation, rather than as a stepwise or discrete positional update. Although the transient solution is solved using discrete time steps, the physical laser motion remains continuous, with time increments selected such that the laser displacement per time step is only a fraction of the beam diameter. Temperature-dependent thermophysical properties for 316L are applied throughout the domain. The powder layer is treated as a continuum with the same properties as the solid. Boundary conditions simulate realistic LPBF conditions. A temperature-dependent convection coefficient models heat loss to the surrounding argon environment, and radiative cooling is included via the Stefan–Boltzmann law. The top surface is exposed to both modes of heat loss, while the lateral and bottom boundaries are thermally insulated. The laser travels along a predefined path at a constant scanning speed. Time steps are selected to ensure that laser movement per step is a fraction of the beam diameter, capturing thermal gradients accurately during heating and cooling.

The finite element model and domain configuration used in this study are shown in Figure 2. The simulation was performed in ANSYS Workbench using a 3D geometry consisting of a 316L stainless steel substrate with a uniform

ISSN: 2149-9373 © 2025 Parantez Academic Publishing All rights reserved

powder layer on top. The mesh consisted of approximately 166,800 elements generated through structured edge sizing, with overall dimensions of 300 × 25 × 25 along the x, y, and z axes, respectively. Mesh defeaturing was enabled to remove geometrical details irrelevant to thermal transport, and a fast transition scheme was employed to ensure a smooth variation of element sizes across the domain. To accurately capture the steep thermal gradients induced by the moving laser, local mesh refinement was applied along the laser scanning path and in the powder–substrate interaction zone, where rapid temperature variations occur. The minimum edge length in the refined region was set to 500 μm, while coarser elements were used away from the melt pool to reduce computational cost. The mesh quality was controlled using ANSYS's mechanical quality metrics with a target element quality of 0.05, and medium smoothing was applied to avoid highly skewed elements and ensure numerical stability. The mesh density in the laser interaction region was selected based on preliminary mesh refinement tests, in which several mesh configurations with progressively finer element sizes were examined. The resulting peak temperatures and melt pool width and depth were compared across these configurations, and it was observed that further mesh refinement led to negligible changes in the predicted thermal field and melt pool geometry, indicating mesh-independent results. Based on this convergence assessment, the final mesh was adopted as an optimal compromise between numerical accuracy and computational efficiency. A transient thermal analysis was conducted with a total simulation time of 4.5 milliseconds, divided into 90 time steps. The numerical solution employed ANSYS's Mechanical APDL (MAPDL) solver. The simulation ran on a computer equipped with an Intel Core i7-12700K processor and 64 GB DDR5 RAM, with a total solution time of approximately 12 minutes for each single-track scan.

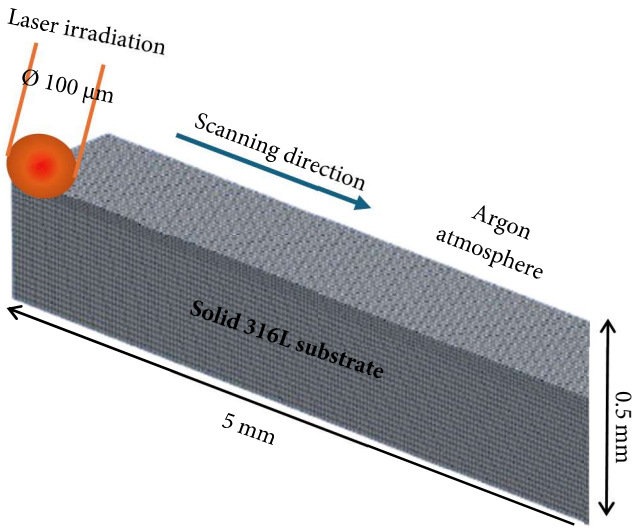


Figure 2. Computational model representing the LPBF process of 316L

2.6. Simulation configuration for laser power variation

This study investigates the effect of laser power on the thermal field and melt pool morphology in LPBF of 316L stainless steel using transient thermal analysis. A single-track scanning model was developed to simulate heat transfer induced by a moving Gaussian volumetric heat source. To assess the thermal response under varying energy input, the simulations were carried out under three different laser power conditions—120 W, 180 W, and 240 W—while keeping other parameters constant. The key parameter used to compare the laser-material interaction conditions is the Volumetric Energy Density (VED), a widely adopted scalar metric in LPBF that estimates the energy input per unit volume of material (as shown in Eq. 6).

$$VED = \frac{P}{v \cdot h \cdot t} \tag{6}$$

where P is the laser power (W), v is the scan speed (mm/s), h is the hatching space (mm), and t is the layer thickness (mm). This formulation provides an effective way to compare energy input levels across different processing conditions,

although it does not account for all thermal transport mechanisms or melt pool dynamics.

In this work, the scanning speed, hatching distance, and layer thickness were kept constant at 1200 mm/s, 0.04 mm, and 0.03 mm respectively. The only variable parameter was the laser power. The three studied power levels—Low (120 W), Optimum (180 W), and High (240 W)—yield VED values of approximately 83.3, 125, and 166.7 J/mm³, respectively, as summarized in Table 2.

Table 2. Laser Processing Parameters

Condition	Laser power (W)	Scanning Speed (mm/s)	Layer Thickness (mm)	Hatching Space (mm)	VED (J/mm³)
High	240	1200	0.03	0.04	166.67
Medium	180	1200	0.03	0.04	125
Low	120	1200	0.03	0.04	83.33

3. Results and Discussion

3.1. Temperature distribution

The transient thermal response of the melt pool was analyzed for three different VED values: Low (83 J/mm³), Medium (125 J/mm³), and High (166 J/mm³), corresponding to varying laser power levels of 120 W, 180 W, and 240 W, respectively. Although Volumetric Energy Density (VED) is a useful scalar parameter for comparing LPBF processing conditions, it may not fully describe melt pool behavior. Different combinations of laser power (P) and scan rate (v) can yield the same VED value while producing different thermal histories and melt pool geometries [22]. In particular, high-power-high-speed and low-power-low-speed combinations may yield the same VED values but lead to differences in melt pool width, depth, and melt mode. In this study, the scan rate was kept constant to isolate the effect of laser power. The temporal evolution of the surface temperature at the laser-material interaction point is presented in Figure 3, where temperature sharply rises upon laser incidence and reaches peak values before decaying rapidly due to heat conduction and convection losses. The peak surface temperatures observed for High, Medium, and Low VED conditions were approximately 3745 °C, 2836 °C, and 2091 °C, respectively. These values reveal a direct and significant influence of energy input on thermal accumulation at the laser–material interface. In the high VED case (166.67 J/mm³), the energy input was sufficient to elevate the surface temperature far above the boiling point of 316L stainless steel (~2927 °C), indicating the likelihood of keyhole-mode melting. At such extreme temperatures, vaporization and recoil pressure effects become dominant, potentially causing instabilities such as pore formation and irregular melt pool boundaries. In the medium VED condition (125 J/mm³), the maximum surface temperature reached 2836 °C—just below the boiling threshold—suggesting stable melting in the transition zone between conduction-mode and incipient keyhole-mode behavior. This range typically enables sufficient melt pool depth and fluidity while minimizing defects like balling or spatter, and thus is considered optimal for process stability. Conversely, the Low VED case (83.33 J/mm³) resulted in a peak temperature of only 2091 °C, slightly above the liquidus temperature of 316L (~1425 °C). This lower energy input limits the melt pool dimensions, risking insufficient fusion between tracks or layers. Incomplete melting under such conditions can lead to lack-of-fusion defects and reduced part density, consistent with experimental findings in earlier studies from Bertoli et al. [27] and Bakhtiarian et al. [15] where insufficient VED values correlated with poor densification and surface quality.

ISSN: 2149-9373 © 2025 Parantez Academic Publishing All rights reserved

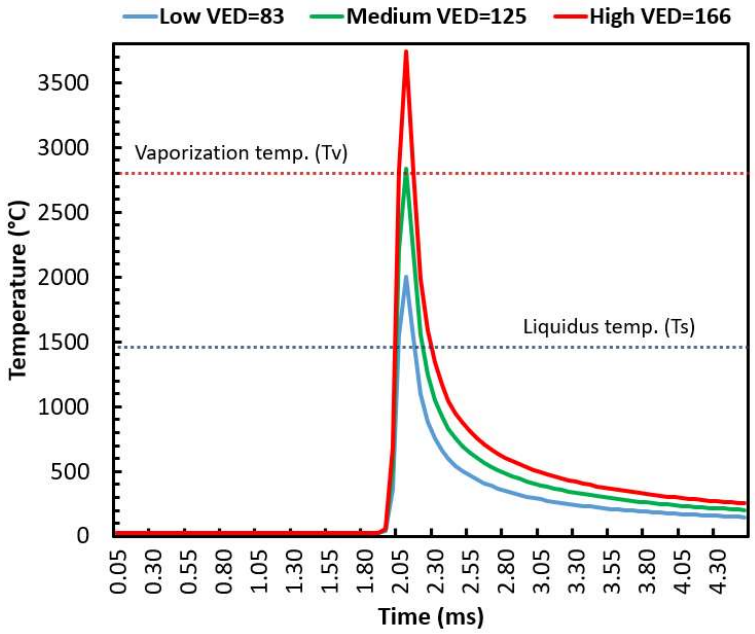


Figure 3. Time-temperature history of a point in the laser interaction zone. Dashed lines indicate Liquidus (T_s) and Vaporization (T_v) temperatures. VED unit: J/mm^3

Figure 4 presents the correlation between laser power and resulting powder surface temperatures, offering a zone-based interpretation of thermal regimes in LPBF processing. As the laser power increases from 120 W to 240 W, the peak surface temperature rises from the liquidus region into the vaporization regime of 316L stainless steel. This trend indicates the gradual change in melting behavior from conduction mode at low power levels to keyhole mode melting at high power levels. The figure visually delineates thermal zones including solid, mushy, liquid, and vapor, reinforcing the notion that fine control over input power is essential to maintain a stable melt pool and avoid defects associated with overheating or under-melting. Unlike Figure 3, which tracks temporal evolution, this figure emphasizes steady-state thermal boundaries and reinforces the importance of operating within a safe thermal window to ensure consistent part quality. The observed thermal transitions and temperature ranges are in agreement with experimental findings reported by researchers such as Bakhtiarian et al. [15], where elevated power levels were shown to induce metal vaporization in 316L stainless steel during SLM processing, thereby supporting the validity of the present simulation model [28].

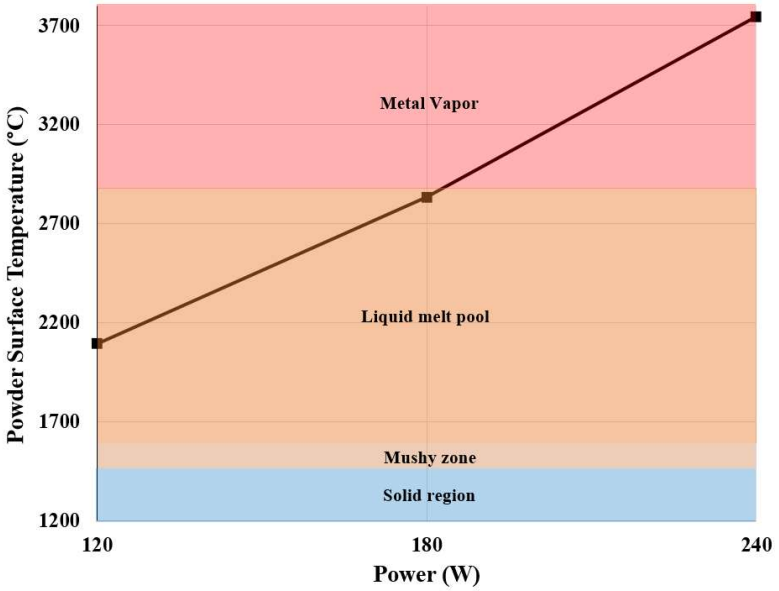


Figure 4. Variation of maximum temperatures reached on the powder surface depending on laser power and phase regions.

Thermal gradient and melt pool morphology are visualized in Figure 5, which shows temperature distributions for different VED values. At low VED (i.e., 83 J/mm^3), a narrower and shallower melt pool is observed, indicating limited penetration and insufficient melting. At medium VED (i.e., 125 J/mm^3), the melt pool expands and deepens, while high VED (i.e., 166 J/mm^3) leads to an enlarged and superheated melt pool, extending thermal influence over a broader region. These thermal field observations support predictions from previous experimental results on 316L SLM fabrication, emphasizing the importance of tightly controlling VED to avoid defects such as lack of fusion or porosity due to vapor-induced instability [16, 27].

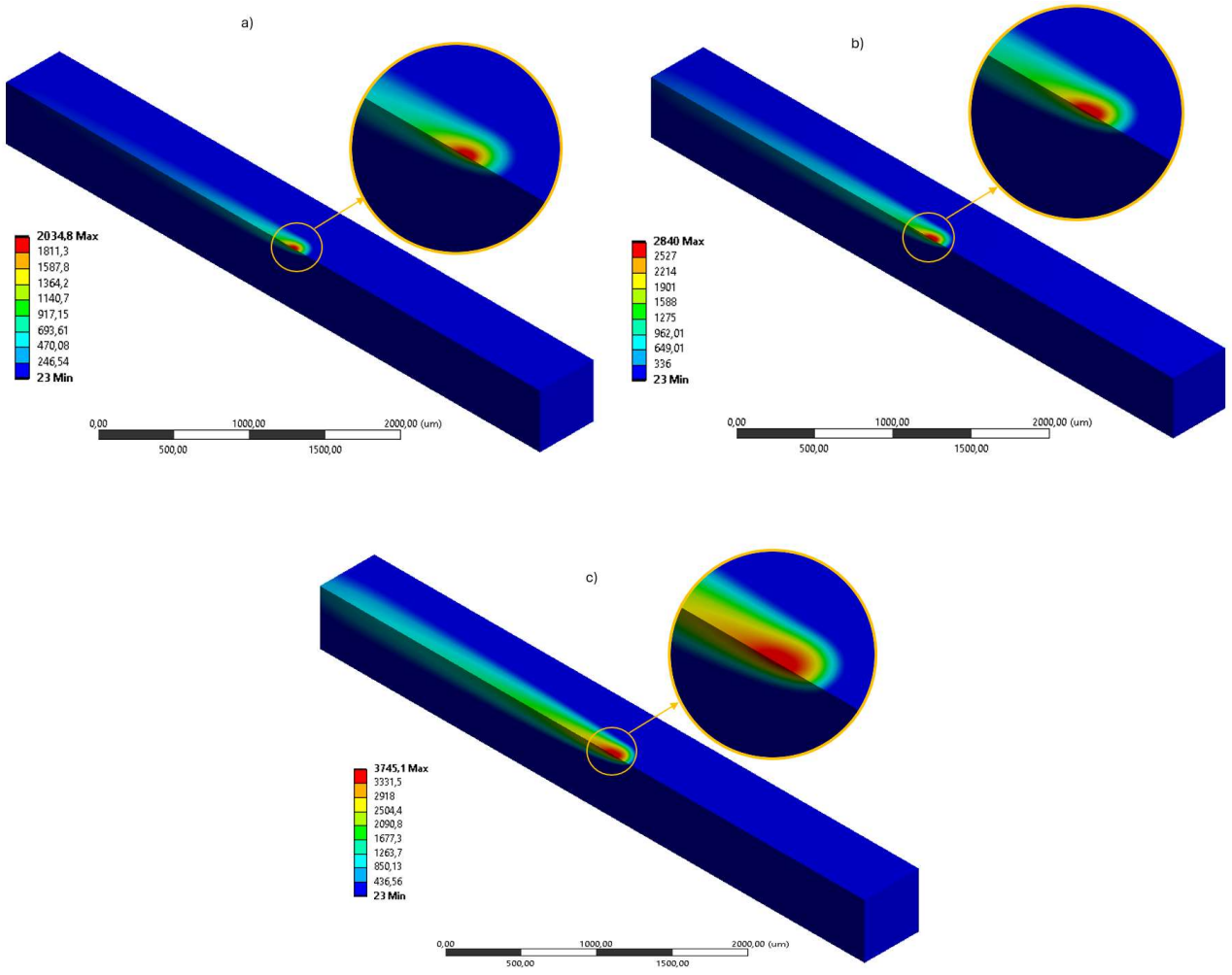


Figure 5. Simulated thermal field distributions and melt pool geometries at different process parameters: a) Low VED, b) Medium VED, c) High VED.

The thermal profiles observed across varying VED levels not only influence the surface temperature response but also play a critical role in governing melt pool morphology. As highlighted in the preceding analysis, peak temperatures vary significantly with energy input, ranging from incomplete melting under low VED to potential vaporization and keyhole formation at high VED. These thermal regimes directly affect melt pool size, shape, and stability, which in turn determine the quality of inter-layer bonding and the presence of defects such as porosity or lack-of-fusion. Understanding this thermal behavior lays the groundwork for analyzing the spatial evolution of the melt pool, which is addressed in the following section.

ISSN: 2149-9373 © 2025 Parantez Academic Publishing All rights reserved

3.2. Melt pool evolution

The morphological characteristics of the melt pool are directly governed by the thermal input, which in this study is modulated through different VED levels. As shown in Figure 6, an increase in VED from 83 to 166 J/mm³ leads to a progressive enlargement in both melt pool width and depth. Under low VED conditions (83 J/mm³), although the peak temperature exceeds the liquidus threshold of 316L (~1425 °C), the resulting melt pool remains shallow, with a depth of only 36 µm. This is marginally greater than the predefined layer thickness of 30 µm used in the simulations, indicating that the molten region does not sufficiently penetrate beyond a single layer. Such minimal overlap poses a high risk of lack-of-fusion defects, especially at interlayer boundaries, where insufficient remelting can result in poor bonding and reduced mechanical integrity. As the VED increases to 125 J/mm³, the melt pool widens to 128 µm and deepens to 58 µm, signifying more efficient energy absorption and heat diffusion into the substrate. At the other end of the energy spectrum, high VED conditions (166 J/mm³) produce a melt pool depth of 96 µm—substantially deeper than the layer thickness and well into the substrate material. This depth, combined with a surface temperature reaching approximately 3745 °C, significantly surpasses the boiling point of 316L stainless steel (~2927 °C) as shown in Table 1. Such extreme thermal inputs can lead to localized vaporization of the material and the formation of a vapor void within the melting pool. This phenomenon is often referred to as keyhole formation. While deeper melt pools are generally favorable for ensuring interlayer fusion, excessive penetration and keyhole instability can introduce gas entrapment and porosity. This risk is especially pronounced under sustained high-power exposure, where melt pool morphology becomes increasingly irregular.

These geometric transitions directly reflect the variation in thermal input described in the previous section, where increasing VED values produced progressively higher surface temperatures. As VED rises, more energy is delivered to the material per unit volume, resulting in an expansion of the melt pool in both width and depth. This correlation is expected, as higher energy input enhances the extent of localized melting and allows heat to penetrate deeper into the substrate. The deepening of the melt pool at higher VED levels is a consequence of more efficient energy absorption and sustained heating, which enlarges the molten zone before solidification occurs. The purely thermal predictions of this study are consistent with trends reported in Bakhtiarian et al [15], confirming that melt pool geometry scales predictably with input energy when process parameters such as scanning speed and layer thickness are held constant.

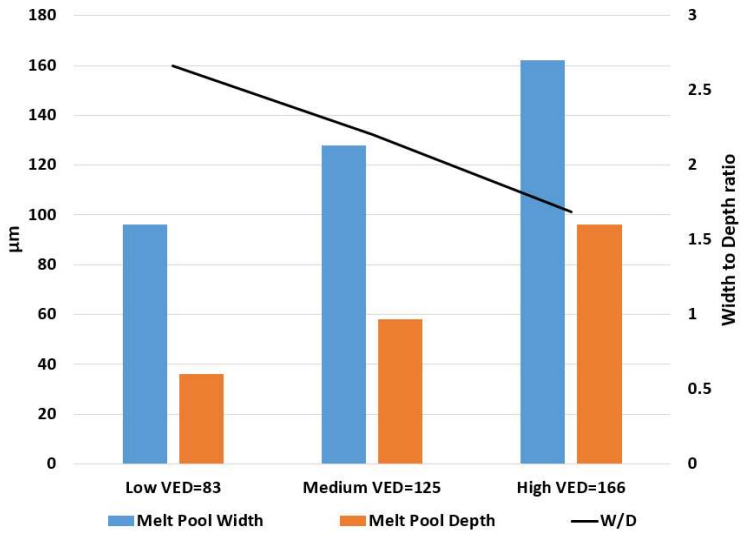


Figure 6. Evolution of melt pool width, depth, and width-to-depth ratio as a function of VED.

A closer analysis of the aspect ratio (width-to-depth) offers deeper insight into the stability and quality of the melt pool. As depicted in Figure 6, the aspect ratio decreases from 2.67 at Low VED to 2.21 at medium and finally to 1.69 at high VED. This inverse relationship between VED and aspect ratio underscores a transition in melting mode. High aspect ratios at low VED indicate predominance of lateral heat spread and shallow penetration, typical of conduction-mode melting. While this condition minimizes the risk of keyhole-induced porosity, it poses a significant risk for lack-of-fusion defects due to insufficient overlap with neighboring tracks. In contrast, the lower aspect ratios observed at higher VED

ISSN: 2149-9373 © 2025 Parantez Academic Publishing All rights reserved

suggest deeper, more columnar melt pools associated with transition to keyhole-mode melting. Such morphologies, although capable of ensuring full fusion, also bring risks of excessive vaporization and porosity if not properly controlled.

Optimizing the melt pool dimensions is therefore essential to ensure structural integrity. Literature suggests that a width-to-depth ratio greater than 2.0 is typically indicative of a stable conduction or transition mode, whereas ratios dropping significantly below 1.5 signal the onset of unstable keyhole formation [27]. In this context, the medium VED condition (125 J/mm^3), yielding an aspect ratio of ~2.2, offers the most favorable balance between adequate penetration depth and geometrical stability. This finding is strongly reinforced by the experimental observations of Bakhtiarian et al. [15], who reported peak relative density (99.5%) and hardness within this specific energy window, confirming that a ratio of ~2.2 avoids the porosity risks associated with deeper, narrower pools.

4. Conclusion

This study presented a computational investigation into the effects of laser power on the thermal behavior and melt pool morphology during LPBF of 316L stainless steel. A transient finite element thermal model was developed to simulate heat conduction induced by a moving Gaussian heat source, excluding fluid flow and phase change effects to achieve high computational efficiency. The results confirm that even simplified thermal models can capture critical trends in LPBF processing and provide actionable guidance on power selection for quality control

Key findings of the study include:

- Surface temperature and melt pool geometry are highly sensitive to VED, with peak temperatures ranging from slightly above the liquidus point (~2090 °C at 83 J/mm^3) to well beyond the vaporization threshold (~3745 °C at 167 J/mm^3).
- Low VED conditions lead to shallow melt pools only marginally deeper than the layer thickness, risking lack-of-fusion defects due to inadequate interlayer bonding.
- At medium VED (125 J/mm^3), a balanced melt pool shape with favorable width-to-depth ratio (~2.2) was achieved, aligning with experimentally validated optimal energy windows for density and hardness.
- Excessive VED values result in deep, narrow melt pools that signal the onset of keyhole formation, which may lead to instability and gas entrapment.

Future research should build upon this framework by incorporating fluid dynamics and phase change models to better resolve melt pool convection, Marangoni flow, and keyhole dynamics. Incorporating multi-track and multi-layer simulations would also help evaluate cumulative thermal effects and remelting phenomena. Moreover, validating the simulation outputs with in-situ thermal imaging or metallographic cross-sections would enhance model accuracy. Finally, extending the parameter space to include scan speed, hatch spacing, and preheat temperature could further enrich the process optimization strategies for defect-free LPBF fabrication of 316L and other alloys.

Conflict of Interest Statement

The authors declare that there is no conflict of interest.

References

[1] S. Chowdhury, N. Yadaiah, C. Prakash, S. Ramakrishna, S. Dixit, L. R. Gupta, and D. Buddhi, "Laser powder bed fusion: a state-of-the-art review of the technology, materials, properties & defects, and numerical modelling," *Journal of Materials Research and Technology,* vol. 20, pp. 2109-2172, 2022. doi: 10.1016/j.jmrt.2022.07.121

[2] D. D. Singh, T. Mahender, and A. R. Reddy, "Powder bed fusion process: A brief review," *Materials Today: Proceedings,* vol. 46, pp. 350-355, 2021. doi: 10.1016/j.matpr.2020.08.415

[3] L. Zhou, J. Miller, J. Vezza, M. Mayster, M. Raffay, Q. Justice, Z. Al Tamimi, G. Hansotte, L. D. Sunkara, and J. Bernat, "Additive manufacturing: a comprehensive review," *Sensors,* vol. 24, no. 9, p. 2668, 2024. doi: 10.3390/s24092668

ISSN: 2149-9373 © 2025 Parantez Academic Publishing All rights reserved

[4] M. Üstündağ, "The Transformative Role of Additive Manufacturing: Current Innovations, Applications, and Future Directions Across Industries," *Duzce University Journal of Science and Technology,* vol. 13, no. 2, pp. 942-963, 2025. doi: 10.29130/dubited.1591082

[5] D. Guillen, S. Wahlquist, and A. Ali, "Critical review of LPBF metal print defects detection: Roles of selective sensing technology," *Applied Sciences,* vol. 14, no. 15, p. 6718, 2024. doi: 10.3390/app14156718

[6] W. H. Kan, L. N. S. Chiu, C. V. S. Lim, Y. Zhu, Y. Tian, D. Jiang, and A. Huang, "A critical review on the effects of process-induced porosity on the mechanical properties of alloys fabricated by laser powder bed fusion," *Journal of Materials Science,* vol. 57, no. 21, pp. 9818-9865, 2022. doi: 10.1007/s10853-022-06990-7

[7] P. Jin, Q. Tang, J. Song, Q. Feng, F. Guo, X. Fan, M. Jin, and F. Wang, "Numerical investigation of the mechanism of interfacial dynamics of the melt pool and defects during laser powder bed fusion," *Optics & Laser Technology,* vol. 143, p. 107289, 2021. doi: 10.1016/j.optlastec.2021.107289

[8] E. Li, Z. Zhou, L. Wang, Q. Zheng, R. Zou, and A. Yu, "Melt pool dynamics and pores formation in multi-track studies in laser powder bed fusion process," *Powder Technology,* vol. 405, p. 117533, 2022. doi: 10.1016/j.powtec.2022.117533

[9] S. Ziri, A. Hor, and C. Mabru, "Combined effect of powder properties and process parameters on the density of 316L stainless steel obtained by laser powder bed fusion," *The International Journal of Advanced Manufacturing Technology,* vol. 120, no. 9, pp. 6187-6204, 2022. doi: 10.1007/s00170-022-09160-w

[10] Z. Hu, S. Gao, L. Zhang, X. Shen, H. L. Seet, S. M. L. Nai, and J. Wei, "Micro laser powder bed fusion of stainless steel 316L: Cellular structure, grain characteristics, and mechanical properties," *Materials Science and Engineering: A,* vol. 848, p. 143345, 2022. doi: 10.1016/j.msea.2022.143345

[11] A. K. Agrawal and D. J. Thoma, "High-throughput surface characterization to identify porosity defects in additively manufactured 316L stainless steel," *Additive Manufacturing Letters,* vol. 3, p. 100093, 2022. doi: 10.1016/j.addlet.2022.100093

[12] X. Chen, W. Mu, X. Xu, W. Liu, L. Huang, and H. Li, "Numerical analysis of double track formation for selective laser melting of 316L stainless steel," *Applied Physics A,* vol. 127, no. 8, p. 586, 2021. doi: 10.1007/s00339-021-04728-x

[13] J. Cherry, H. Davies, S. Mehmood, N. Lavery, S. Brown, and J. Sienz, "Investigation into the effect of process parameters on microstructural and physical properties of 316L stainless steel parts by selective laser melting," *The International Journal of Advanced Manufacturing Technology,* vol. 76, no. 5, pp. 869-879, 2015. doi: 10.1007/s00170-014-6297-2

[14] E. Liverani, S. Toschi, L. Ceschini, and A. Fortunato, "Effect of selective laser melting (SLM) process parameters on microstructure and mechanical properties of 316L austenitic stainless steel," *Journal of Materials Processing Technology,* vol. 249, pp. 255-263, 2017. doi: 10.1016/j.jmatprotec.2017.05.042

[15] M. Bakhtiarian, H. Omidvar, A. Mashhuriazar, Z. Sajuri, and C. H. Gur, "The effects of SLM process parameters on the relative density and hardness of austenitic stainless steel 316L," *Journal of Materials Research and Technology,* vol. 29, pp. 1616-1629, 2024. doi: 10.1016/j.jmrt.2024.01.237

[16] K. Fri, I. Akhrif, A. Laazizi, M. El Jai, M. Bensada, and A. Ouannou, "Experimental investigation of the effects of processing parameters and heat treatment on SS 316L manufactured by laser powder bed fusion," *Progress in Additive Manufacturing,* vol. 9, no. 6, pp. 1787-1809, 2024. doi: 10.1007/s40964-023-00538-0

[17] T. Mukherjee, H. Wei, A. De, and T. DebRoy, "Heat and fluid flow in additive manufacturing–Part II: Powder bed fusion of stainless steel, and titanium, nickel and aluminum base alloys," *Computational Materials Science,* vol. 150, pp. 369-380, 2018. doi: 10.1016/j.commatsci.2018.04.027

[18] R. Acharya, J. A. Sharon, and A. Staroselsky, "Prediction of microstructure in laser powder bed fusion process," *Acta Materialia,* vol. 124, pp. 360-371, 2017. doi: 10.1016/j.actamat.2016.11.018

[19] P. Foteinopoulos, A. Papacharalampopoulos, and P. Stavropoulos, "On thermal modeling of Additive Manufacturing processes," *CIRP Journal of Manufacturing Science and Technology,* vol. 20, pp. 66-83, 2018. doi: 10.1016/j.cirpj.2017.09.007

[20] M. Ansari, M. Khamooshi, Y. Huang, and E. Toyserkani, "Analytical solutions for rapid prediction of transient temperature field in powder-fed laser directed energy deposition based on different heat source models," *Applied Physics A,* vol. 127, no. 6, p. 445, 2021. doi: 10.1007/s00339-021-04591-w

[21] Y. Zhang, V. Shapiro, and P. Witherell, "Towards thermal simulation of powder bed fusion on path level," in *International Design Engineering Technical Conferences and Computers and Information in Engineering Conference*, 2019, vol. 59179: American Society of Mechanical Engineers, California, USA [Online]. doi: 10.1115/DETC2019-98046

[22] O. Eren, "3D Multi-Physics Finite Element Simulation of the Selective Laser Sintering Process for Polyamide 12: Effects of Laser Parameters on Melt Pool Formations and Sintering Quality," *Macromolecular Theory and Simulations,* p. e00094, 2025. doi: 10.1002/mats.202500094

ISSN: 2149-9373 © 2025 Parantez Academic Publishing All rights reserved

[23] I. La Fé-Perdomo and J. A. Ramos-Grez, "An insight into adiabatic efficiency hybrid modeling in Laser-Based Powder Bed Fusion of 316L stainless steel," *Optics & Laser Technology,* vol. 161, p. 109203, 2023. doi: 10.1016/j.optlastec.2023.109203

[24] K. C. Mills, *Recommended Values of Thermophysical Properties for Selected Commercial Alloys*, Woodhead Publishing, 2002, pp. 135-142.

[25] A. B. Alquaity and B. S. Yilbas, "Investigation of spatter trajectories in an SLM build chamber under argon gas flow," *Metals,* vol. 12, no. 2, p. 343, 2022. doi: 10.3390/met12020343

[26] K. Avegnon, A. Menendez, J. Liu, Y. Mittal, K. Karunakaran, and M. Sealy, "Patterned keyhole porosity formation in laser powder bed fusion caused by local disturbances in the shielding gas flow," *Manufacturing Letters,* vol. 35, pp. 677-682, 2023. doi: 10.1016/j.mfglet.2023.08.073

[27] U. S. Bertoli, A. J. Wolfer, M. J. Matthews, J.-P. R. Delplanque, and J. M. Schoenung, "On the limitations of volumetric energy density as a design parameter for selective laser melting," *Materials & Design,* vol. 113, pp. 331-340, 2017. doi: 10.1016/j.matdes.2016.10.037

[28] G. O. Barrionuevo, J. Ramos-Grez, M. Walczak, and I. La Fé-Perdomo, "Numerical analysis of the effect of processing parameters on the microstructure of stainless steel 316L manufactured by laser-based powder bed fusion," *Materials Today: Proceedings,* vol. 59, pp. 93-100, 2022. doi: 10.1016/j.matpr.2021.10.209

This is an open access article under the CC-BY license